

# Large Band-Edge Photocurrent Peak in Thick Methylammonium Lead Iodide Photosensors with Symmetric Metal Electrodes

Péter Hantz,<sup>\*,||</sup> Ferenc Sarlós,<sup>‡</sup> István Jalsovszky,<sup>§</sup> and Balázs Plesz<sup>⊥</sup>

<sup>||</sup>Department of Laboratory Medicine, University of Pécs, Medical School, Ifjúság útja. 13, H-7624 Pécs, Hungary

<sup>‡</sup>Institute of Biophysics, Biological Research Centre of the Hungarian Academy of Sciences, Temesvári krt. 62, H-6726 Szeged, Hungary

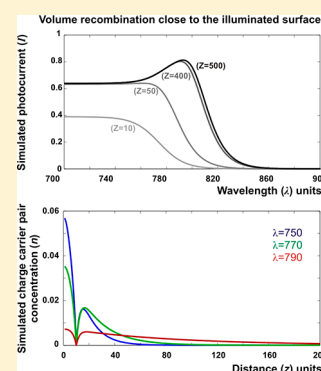
<sup>§</sup>Department of Organic Chemistry, Institute of Chemistry, Eötvös Loránd University, Pázmány Péter sétány 1/A, H-1117 Budapest, Hungary

<sup>⊥</sup>Department of Electron Devices, Budapest University of Technology and Economics, Magyar Tudósok körútja 2, H-1117 Budapest, Hungary

## Supporting Information

**ABSTRACT:** This study examines the photocurrent (photoconductivity) spectra of thick methylammonium lead iodide perovskite layers coupled to symmetric metal electrodes. A large photocurrent peak has been observed in the near-band-gap wavelength region. The origin of this current peak is related to an interplay between the penetration depths of light having a certain wavelength and its ability to raise the concentration of the charge carriers. A model including the generation, position-specific or uniform recombination, as well as diffusion of charge carrier pairs, made it possible to reproduce the experimental findings. Besides the microscopic approach, we also present a phenomenological model and a simulation providing the conductance for an arbitrary relative orientation of the illuminating beam and the field imposed by the electrodes. The results enabled us to outline the functioning principle of a sensor for determining the angle of incidence of electromagnetic radiation. Furthermore, a method for estimating optical absorption spectra from photocurrent spectra is delineated.

**KEYWORDS:** photocurrent spectroscopy, near-band-gap peak, lead halide perovskite, optical absorption, radiation direction sensor, reaction–diffusion model



Photocurrent spectroscopy is a versatile tool for studying optoelectronic processes in semiconductors. In this paper, we perform time-domain dc photocurrent (photoconductivity) spectroscopy by exposing a photoconductive sample to monochromatic light with sweeping frequency, while the specimen is kept under a steady potential difference. The record represents the wavelength-dependent photocurrent originating from photoinduced free charge carriers. For certain semiconductor samples, a photocurrent increase might be observed for near-band-gap frequencies of the illuminating light. This current peak may emerge due to several reasons, while its characteristics offer important insight into the electronic properties of the material.

A possible physical reason for this phenomenon is the wavelength-dependent penetration depth and charge carrier generation ability of the illumination. This idea was first described in the classic paper of DeVore<sup>1</sup> and was later further investigated by including different boundary conditions.<sup>2,3</sup> These models assume that the potential difference is perpendicular to the direction of the illuminating light beam. Layers at growing depths compared to the illuminated interface are exposed to decreasing light intensity and therefore have increasing resistance. The overall conductivity of the sample is computed by adding the conductivities of the individual layers.

Therefore, the sample conductivity as a function of the wavelength, meaning the photocurrent (photoconductivity) spectrum, is not proportional to the optical absorption spectrum of the material.

The photocurrent peak can also originate from the photogeneration of excitons, a process that demands a slightly lower amount of energy than the band gap. The formation of these quasiparticles may also manifest as a near-band-gap peak in the optical absorption spectrum.<sup>4,5</sup> Although excitons do not carry charge themselves, they may dissociate into electrons and holes, especially if their binding energy is not much higher than the thermal energy  $kT$ . Most of the halide perovskites show a distinct excitonic peak in the optical absorption spectrum, even at room temperature. However, the methylammonium lead iodide, which is the objective of our research, does not show this feature (or shows it only very weakly) at ambient conditions. The excitonic peak in methylammonium lead triiodide (MAPbI<sub>3</sub>) becomes significant only at low temperatures.<sup>6,7</sup>

Interpreting the outcome of photocurrent (photoconductivity) spectroscopy on organometal halide perovskites is of

Received: March 18, 2017

special importance, since these organic–inorganic semiconductors exhibit a series of attractive properties for photovoltaics and optoelectronics.<sup>8–10</sup> They can be prepared through easy and cheap solution processing, which results in solid perovskite phases of various types and crystalline structure, spanning from spin-coated thin polycrystalline layers to single crystals in the centimeter range.<sup>11–14</sup> A further advantage is the straightforward band-gap tuning by appropriate selection of the cation or using a mixture of halide ions.<sup>15–17</sup>

In comparison with the vast majority of studies on organometal halide perovskites, we investigated thick layers of methylammonium lead triiodide, where the penetration depth of near-band-gap photons is much smaller than the thickness of the sample (which was about 8  $\mu\text{m}$ ). Using a simple toolkit, we describe and successfully model an unusual photocurrent peak observed at the red edge of the absorption spectrum of a thick  $\text{MAPbI}_3$  layer with symmetric metal electrodes. On the basis of this effect, we propose a very simple electro-optical sensor for determining the irradiation direction of a light beam. Moreover, the model enables us to estimate the optical absorption spectrum from the photocurrent spectrum in the wavelength range where the absorption spectrum cannot be recorded.

## METHODS

**Sample Preparation.** Manufacturing custom layers of  $\text{MAPbI}_3$  is a process of several stages. First, random-shaped crystals are produced. Subsequently these are dissolved in dimethylformamide (DMF,  $(\text{CH}_3)_2\text{NCHO}$ ), resulting in a solution that can easily be handled to yield polycrystalline  $\text{MAPbI}_3$  at a desired location and with an appropriate shape.

We commence by dissolving 10 mM (4.61 g)  $\text{PbI}_2$  crystals in 9 mL of 57 wt % HI solution (corresponding to 69.1 mM HI) by heating to about 100  $^\circ\text{C}$ . The resulting yellow liquid is cooled to room temperature. No crystals will appear at this time (Figures S1 and S2 and technical details in the [Supporting Information](#)).

Next, we add 10 mM (1.59 g) crystalline  $\text{CH}_3\text{NH}_3\text{I}$  (same molarity as the  $\text{PbI}_2$ ) to the above solution. Seeds of black  $\text{MAPbI}_3$  crystals will immediately emerge (Figure S3 in the [Supporting Information](#)).

Subsequently, the mixture is heated to 100  $^\circ\text{C}$ , and a 57 wt % HI solution is added to it during continuous heating, until the black precipitate dissolves. Afterward, the solution is allowed to cool to room temperature, and during the cooling process, millimeter-sized  $\text{MAPbI}_3$  crystals form (Figure S4 in the [Supporting Information](#)). Recrystallization in a spatial temperature gradient, approximately between 30 and 70  $^\circ\text{C}$ , yields larger crystals.

$\text{MAPbI}_3$  crystals were harvested from the solution, spread on a glass filter, gently rinsed with chloroform or diethyl ether, and dried by  $\text{N}_2$  gas flow. Finally, they were heated for 30 min to 120  $^\circ\text{C}$  to remove all solvents. Resulting  $\text{MAPbI}_3$  grains were stored in a desiccator (Figure S5 in the [Supporting Information](#)). Some of the crystals were fractioned and checked by X-ray powder diffraction (Figure S7 in the [Supporting Information](#)).

In the second step, 0.5 g of the harvested grains was dissolved in 1 mL of DMF. This way, a perfect stoichiometry is guaranteed. This solution can unlimitedly be stored in closed vessels.

Symmetric copper, platinum, and gold electrodes were deposited on 1 mm thick 25  $\times$  25 mm glass plates by evaporation or sputtering. The electrodes had either a

rectangular shape, placed at a distance of 5 mm, or an interdigitated structure, with 1 mm, 300  $\mu\text{m}$ , or 500  $\mu\text{m}$  gaps.

To prepare spin-coated samples, 50  $\mu\text{L}$  of  $\text{MAPbI}_3$  solution was dropped at room temperature on the glass plate with the electrodes spinning with a speed of 4000 rpm for 20 s. After a couple of seconds, the same amount of toluene was dropped on the sample to extract most of the solvent. This way, a uniform polycrystalline layer with about 70 nm thickness formed.

Perovskite layers with a maximal thickness of 50  $\mu\text{m}$  were manufactured as follows: 4 to 6  $\mu\text{L}$  of the  $\text{MAPbI}_3$  dissolved in DMF was dropped on the glass plate with electrodes and allowed to dry at about 40  $^\circ\text{C}$ . First a white, and subsequently a gray, polycrystalline phase was formed. To facilitate the evaporation of the DMF, the sample was heated to 110–130  $^\circ\text{C}$  for 5 min (Figure S6 in the [Supporting Information](#)). The resulting crystals were also checked by X-ray fluorescence (Figure S7 in the [Supporting Information](#)).

In order to protect and conserve the moisture-sensitive perovskite, viscous poly(methyl methacrylate) (PMMA) dissolved in toluene was layered on the sample, which was capped by a microscope cover glass.

## Photocurrent (Photoconductivity) Spectroscopy.

Spectroscopic investigations were carried out between 720 and 920 nm. The light beam falling on the sample was adjusted in the entire wavelength interval to uniform power values. Experiments carried out with uniform photon numbers led to similar results. The beam had a Gaussian profile independent of the wavelength, with a mean standard deviation of 0.9 mm (Figure S8 in the [Supporting Information](#), where the peak power densities of the applied power values are also given). Illumination of 1.2 s was followed by a dark period of 3 s, while the wavelength was increased in each cycle by 5 nm (Figure S9 in the [Supporting Information](#)). A SpectraPhysics MaiTai eHP DeepSee titanium-sapphire laser was used as a light source, in continuous wave (CW) or pulsed wave (PW, repetition rate 80 MHz, pulse duration 70 fs) mode. No photoconductivity difference was observed while illuminating the sample with PW or CW light of the same power. The type (interdigitated or square) or the material (copper, gold, or platinum) of the electrodes and the presence or absence of the PMMA coverage did not influence the outcome of the experiments. Dependence of the photocurrent on the applied voltage in the 0.1 to 20 V range was, with a good approximation, linear.

Further details of the illumination system are presented in the [Supporting Information](#). Current through the sample was recorded by a Keithley 2400 SourceMeter in a four-point configuration at various constant voltages between 0.1 and 10 V and with a temporal resolution of 0.2 point/s. Most experiments were carried out at 5 V. Voltage–current hysteresis was negligible. Data acquisition was controlled by custom-made Labview software. Time points when the light was turned on and off were specified by registering the current change of a photodiode placed at the end of the light path.

## RESULTS

**Experimental.** The photocurrent spectra of uneven  $\text{MAPbI}_3$  samples with a nonuniform thickness of an average of about 8  $\mu\text{m}$  exhibit a characteristic shape: close to the band gap (1.55 eV, corresponding to a wavelength of 800 nm), a large current peak emerges (Figure 1, colored curves). The peak position and amplitude show a variation from sample to sample. They can vary even if different regions are illuminated within the same sample. By increasing the wavelength,

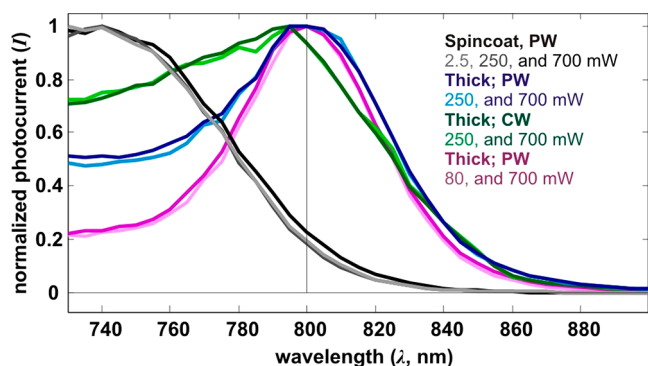


**Figure 1.** Photocurrent (photoconductivity) spectra of sensors with perovskite layers having different thicknesses. Currents were normalized to a peak value equaling 1. Type of MAPbI<sub>3</sub> layer and type and power of illumination are individually noted. CW, continuous wave; PW, pulsed wave. The Gaussian beam profile had a standard deviation of 0.9 mm, with average peak power densities ranging from 0.046 to 12.9 W/cm<sup>2</sup> (for 2.5 and 700 mW beam power, respectively). The potential difference applied on the sample was 5 V.

photocurrent values start to grow at 720 nm and to decrease at 800 nm. However, sensors with a thin (less than 100 nm) spin-coated perovskite layer showed no peak at all or just a tiny peak, which is similar to the data presented in the mainstream literature<sup>18</sup> (Figure 1, gray curves).

It is important to mention that *optical absorption spectra* of the sample did not show any increase around the band gap or any other discrepancy from the usual MAPbI<sub>3</sub> spectra. Note that our thick (not spin-coated) sensors had an uneven thickness. In most parts they were more than 1 μm thick and therefore completely blocked the visible light, while in other locations they were pitted; the samples were not optimized for obtaining high-quality optical absorption spectra.<sup>19</sup>

**Phenomenological Modeling.** Our phenomenological model explains photocurrent spectra for an arbitrary orientation of the electric field with respect to the illuminating light beam. However, only two qualitatively different circumstances are of special interest, namely, those in which the illuminating light beam is parallel<sup>20</sup> or perpendicular<sup>18</sup> to the applied electric field.

The “parallel” arrangements can be modeled by a series of different conductances coupled in series. “Perpendicular” arrangements can be modeled by conductances coupled in parallel (Figure 2). Therefore, in the “perpendicular” case, photoconductance will appear even if only one layer is conductive, while in the “parallel” one, the high resistance of

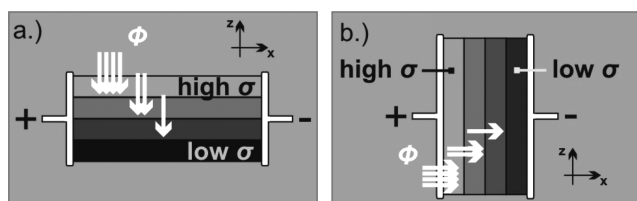


**Figure 2.** (a) “Perpendicular” arrangement. Upper layers are more conductive if illuminated with photons having a larger energy than the band gap. The overall conductance can be modeled by conductances of individual layers coupled in parallel. (b) “Parallel” arrangement. Left layers are more conductive if the setup is illuminated as shown in the figure. The overall conductance can be modeled by conductances of individual layers coupled in series.

a single layer can obstruct the photocurrent flow (and only a minor dark current will pass through the electrodes). Note that this model holds for a case where the conductance of a layer is mainly determined by the amount of the absorbed light, and charge carrier diffusion length, that is, the recombination distance, is much smaller than the sample thickness.

The phenomenological model successfully describes the most important aspect of the experimental results in our perpendicular arrangement with thick samples, namely, the emergence of the photocurrent peak. However, it does not account for the effects induced by highly uneven samples.

As an input, the model requires the absorption coefficient of the material as a function of the wavelength. This can be determined experimentally (Figure S10 in the Supporting Information), but with a good approximation one can assume that it is a sigmoidal curve that is centered on the wavelength where the optical absorption has the most abrupt decrease. The model also assumes that the number of photons absorbed in a certain depth follows the Bouguer–Beer–Lambert law.<sup>21</sup> Besides the straightforward issues mentioned above, the model has two further assumptions. First, the conductance of a layer with unit thickness and in a certain depth is given as follows: the product of the photons reaching the layer and the absorbance at the wavelength of the incident photons is raised to a power  $\gamma$ , which represents a free parameter. Second, the conductance of the entire sample is computed by summing the conductances of the individual layers. Note that our assumptions implicitly demand a stationary charge carrier distribution within the sample.

The phenomenological model is implemented by three equations. The wavelength-dependent absorbance  $A(\lambda)$  is given by

$$A(\lambda) = \frac{K}{C + e^{\alpha(\lambda-770)}} \quad (1)$$

where  $K$ ,  $C$ , and  $\alpha$  are the parameters of the optical absorption spectrum.

The photon density at a given wavelength  $\lambda$  and depth  $z$ , assuming unit value at  $z = 0$ , reads

$$\Phi(\lambda, z) = e^{-A(\lambda)z} \quad (2)$$

The current generated at the depth  $z$ , for a certain fixed voltage, is given by

$$j(\lambda, z) = [\Phi(\lambda, z) A(\lambda)]^\gamma \quad (3)$$

where  $\gamma$  is the free parameter.

Representative outcomes of the model for flat sample with different thicknesses in a perpendicular arrangement are shown in Figure 3. Note the fact that by decreasing the thickness of the modeled sample the peak gradually disappears. The absence of the peak in the experiments performed with a thin and uniform spin-coated sample confirms the finding that the photocurrent peak emerges only above a certain sample thickness. Fine tuning of the sample dimensions and the experimental confirmation of the predicted shift of the peak characteristics as a function of the sample thickness is in progress. However, these effects emerge in the microscopic model presented below.

In our experiments and simulations we also found a significant photocurrent tail below the band gap. The *optical absorption* in this wavelength range is referred to as the Urbach tail.<sup>22</sup> However, due to the nonlinear relationship between the

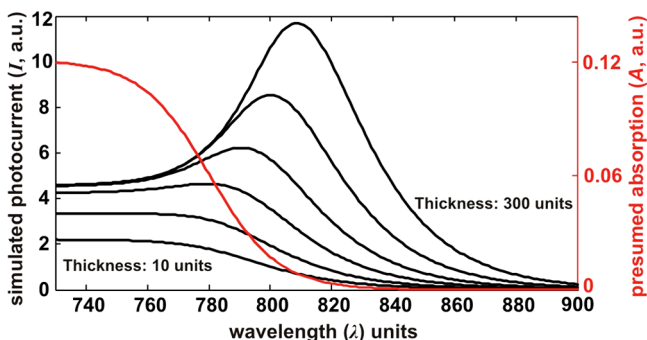


**Figure 3.** Simulated photocurrent spectra for semiconductor layers with different thicknesses, in “perpendicular” arrangement. The presumed absorption spectrum is plotted in red. Parameters:  $C = 2.5$ ,  $\alpha = 0.09$ ,  $K = 0.3$ , the sigmoid representing the absorption spectrum is centered at 770 units corresponding to the wavelength, while  $\gamma = 0.55$ . Values of  $Z$ , corresponding to the thickness, are 10, 20, 40, 75, 150, and 300 units.

absorbance and the total photocurrent of thick samples, photocurrent (photoconductivity) spectroscopy in the sub-band-gap region is more sensitive than the optical spectroscopy.

Despite the simplicity of the phenomenological model, we managed to fit three representative experimental results, varying only the thickness  $Z$  and the parameter  $\gamma$  (Figure 4). At this

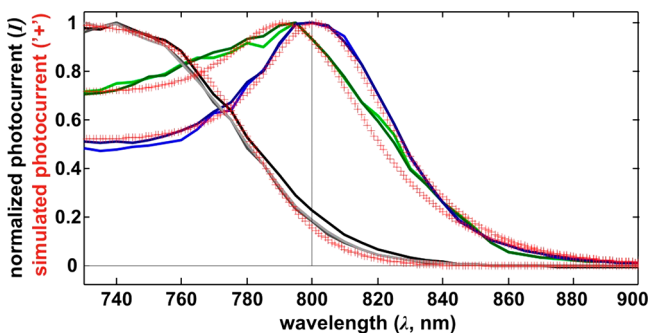


**Figure 4.** Fitting simulated photocurrent spectra (traces of red crosses) to experimental results (continuous curves). Parameters defining the absorption spectrum were kept constant ( $C = 2.5$ ,  $\alpha = 0.09$ ,  $K = 0.3$ ), while only  $\gamma$  and sample thickness  $Z$  were altered. For fitting the gray, green, and blue curves, these were ( $Z = 1$ ,  $\gamma = 1$ ), ( $Z = 75$ ,  $\gamma = 0.5$ ), and ( $Z = 160$ ,  $\gamma = 0.55$ ).

time we do not have a full physical understanding of this parameter, but the subsequent microscopic model revealed its relationship to the spatial distribution of the recombination sites.<sup>23</sup> Note that the model fits only the photocurrent curves with a peak having a simple bump-like increase and decrease (like in Figure 4, Figure 8a–c, and Figure S11e). We emphasize that all experimentally obtained curves fulfill this requirement. The dimensionless form of the model is presented in the Supporting Information.

Our numeric approach is operable for any illumination angle hitting a cuboid-shaped sensor. Figure 5 shows the photocurrent spectrum obtained for a “parallel” configuration, that is, when the (simulated) light beam falling on the cuboid sample is in line with the electric field. The light is assumed to fall on and penetrate into the sample through a transparent electrode. This simulation rectifies some results reported on a “parallel” configuration.<sup>24</sup>

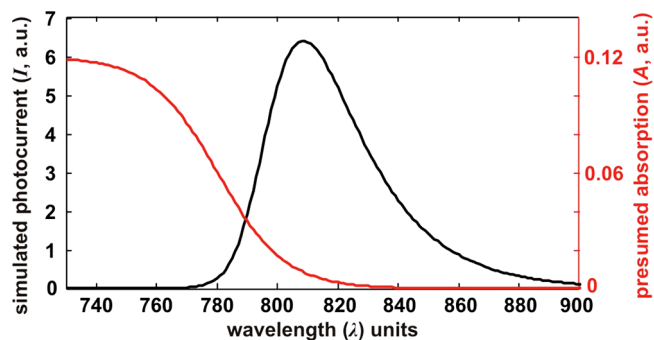


**Figure 5.** Simulated photocurrent (photoconductivity) spectrum for parallel arrangement. Note the negligible photocurrent on the sides of the shown wavelength interval. The presumed absorption spectrum is plotted with a dashed red line.  $C = 2.5$ ,  $\alpha = 0.09$ ,  $K = 0.3$ , and  $\gamma = 0.55$ . Sample length was  $x = 200$  units.

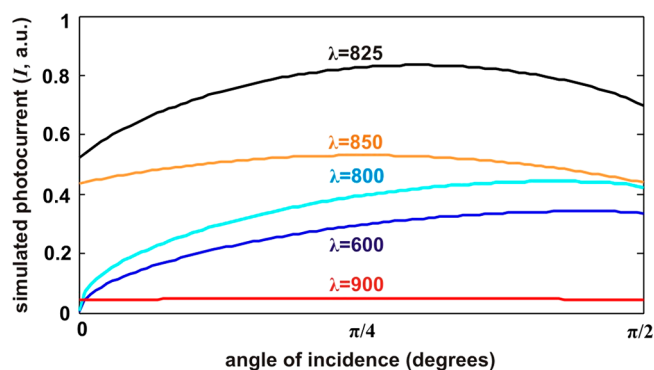


**Figure 6.** Simulated dependence of the photocurrent on the angle of incidence and on the wavelength. The model is based on eq 3 for a cubic sample with transparent electrodes. Parameters are the same as for the preceding simulations. The angle of incidence varies from 0 (“parallel” beam) to  $\pi/2$  (“perpendicular” beam). As the parameter corresponding to the wavelength (photon energy) increases through the band gap, the light penetrates more uniformly in the sample and the angle dependence vanishes.

**Illumination from an Arbitrary Direction.** Simulated dependence of the photocurrent intensity on the angle of incidence in the  $[0, \pi/2]$  range, for a cuboid sample with a transparent electrode, is presented in Figure 6. Here we modeled the effect of various monochromatic illumination with the same intensity. Five different wavelengths, namely, two below, one at, and two above the band gap, were investigated (for the computational implementation, see the Supporting Information). This result demonstrates that a thick semiconductor layer equipped with symmetric metal electrodes could serve as a sensor or part of a device detecting the direction of incidence of electromagnetic radiation with a known intensity and spectrum, provided that the radiation includes a substantial amount of over-band-gap photons.

Present-day devices developed to determine the direction of electromagnetic radiation involve shielding, gratings, collimators, or other optical elements,<sup>25–31</sup> while the sensor proposed in this paper consists of only a semiconductor cuboid equipped with transparent or nontransparent electrodes. Due to their heavy elements, sensors consisting of halide perovskites could even serve for determining the directionality of X- or  $\gamma$ -rays.<sup>32–36</sup> We have to mention that modeling X- or  $\gamma$ -ray detection needs a different theoretical approach. Note that a single sensor with two transparent electrodes delivers only

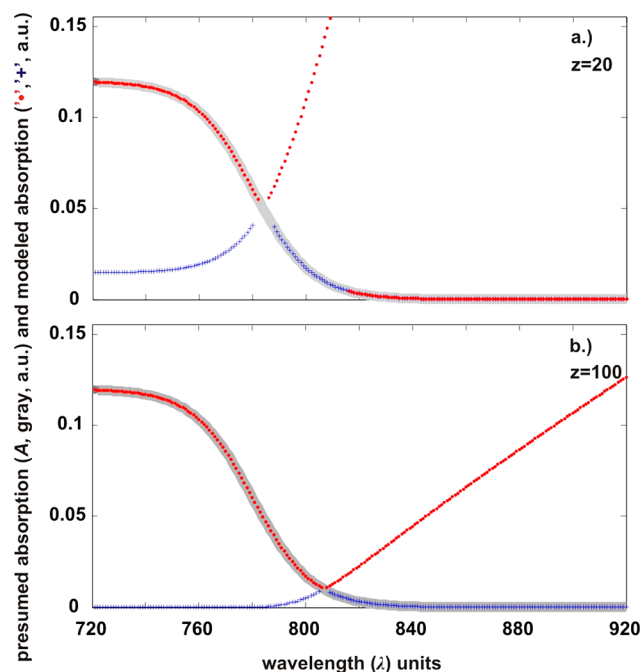


**Figure 7.** Assumed optical absorption spectrum (thick gray sigmoidal line) and its reconstruction from simulated photocurrent spectra of samples with different thicknesses. Red and blue curves represent the solutions of eq 5. Curves in (a) and (b) are derived from model samples with thicknesses of 20 and 100 units. The remaining simulation parameters are  $C = 2.5$ ,  $\alpha = 0.09$ ,  $K = 0.3$ , and  $\gamma = 0.55$  (the same as for Figure 3).

uniaxial data and cannot discriminate between angles symmetric to the perpendicular. Moreover, the sensor is functional only if spectral and intensity information is available.

### Reconstructing the Optical Absorption Spectrum from the Photocurrent (Photoconductivity) Spectrum.

The model offers the possibility to estimate the absorption spectrum  $A(\lambda)$  from the photocurrent spectrum  $I(\lambda, z)$ . Due to the nonlinear relationship between the optical absorbance and the total photocurrent of thick samples, photocurrent spectroscopy is very sensitive even in the sub-band-gap region.<sup>37</sup> Having an appropriate model, the method could be used to obtain or to approximate the absorption spectrum in the domain where the classical methods are uncertain, e.g., at photon energies below the band gap.

Let us consider a “perpendicular” experimental configuration and assume that the photocurrent spectrum is recorded for a series of cuboid samples with varying total thickness  $Z$ . According to our model, the total photocurrent reads

$$I(\lambda, Z) = \int_0^Z [e^{-A(\lambda)z} A(\lambda)]^\gamma dz \quad (4)$$

Differentiating it with respect to the upper limit and subsequently raising the result to the power  $1/\gamma$ , we have

$$Y(\lambda, Z) = \left[ \frac{d}{dZ} I(\lambda, Z) \right]^{(1/\gamma)} = A(\lambda) e^{-A(\lambda)Z} \quad (5)$$

which allows finding  $A(\lambda)$ , from  $I(\lambda, Z)$  numerically or through the Lambert  $W$  function. More precisely, we obtain a series of expressions for the absorption which depend on  $\lambda$  and the parameter  $Z$ , which allow assembling  $A(\lambda)$ . Since the expression on the right side is a peak shape function, the equation has two

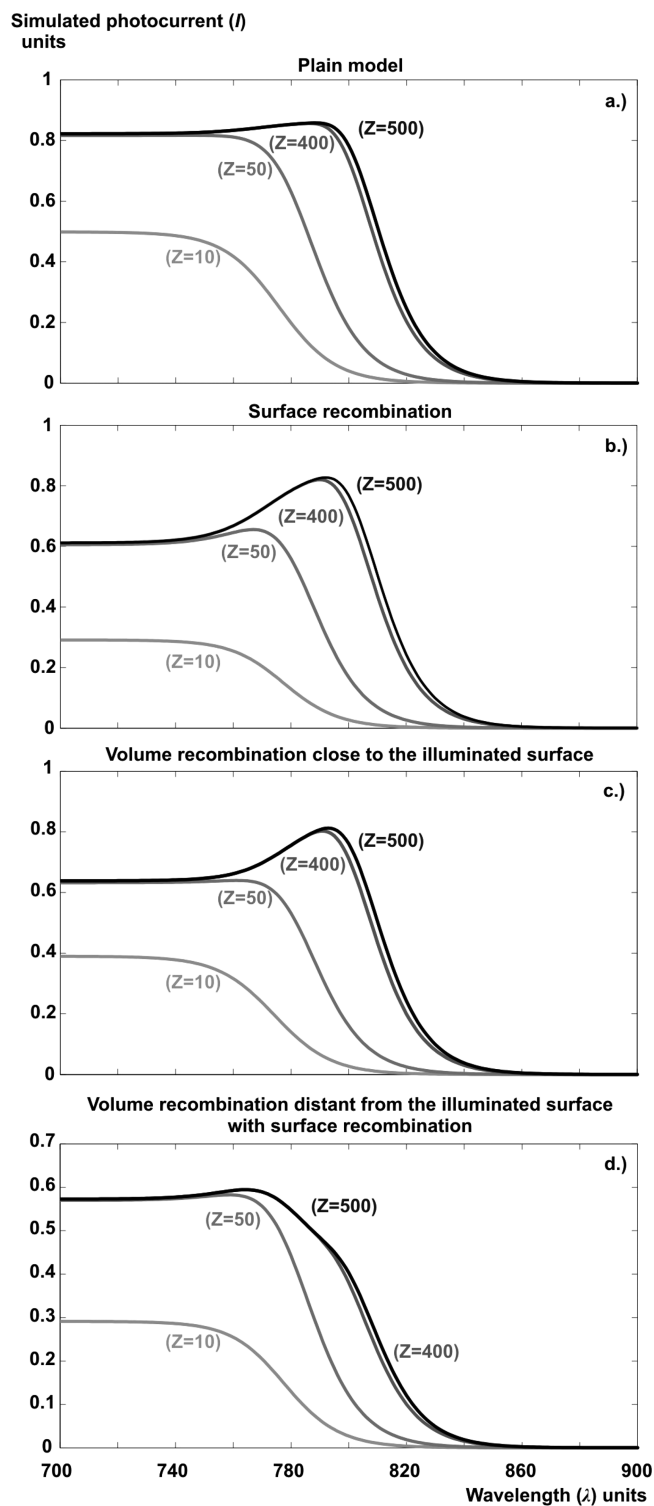


**Figure 8.** Simulated photocurrent (photoconductivity) spectra resulting from the reaction–diffusion model. (a) No recombination sites (where  $n = 0$ ) are present. The peak at the band edge is moderate. (b) Recombination site placed at the illuminated surface; a strong peak emerges. (c) Peak with a similar magnitude can be implemented by locating a recombination site in the volume, but close to the illuminated surface. (d) Additionally to a surface recombination site, a series of volume recombination sites, farther from the illuminated surface, are also present. These latter will significantly decrease the photocurrent peak. Curves with different shades of color represent the photocurrent spectra of models with different thickness  $Z$ , marked next to each curve. The expression of the assumed

Figure 8. continued

sigmoidal light absorption is  $A(\lambda) = 0.1/(1 + e^{(0.1(\lambda-770))})$ . Parameters:  $\tau^{-1} = 0.1$ ,  $D = 1$ ,  $dz = 1$ ,  $dt = 0.01$ ; the sample thickness was 500 units, and 2000 iterations were performed. Note that the curves suffered only minor alterations after 1000 iterations. The recombination sites are  $z = 1$  (b),  $z = 10$  (c), and  $z = [1, 30, 40, \dots, 500]$  (d). The corresponding densities of the charge carrier pairs are shown in Supporting Figure S12.

solutions for  $A(\lambda)$ . Numerical simulations (for details, see the Supporting Information) showed that the physical solution is a piecewise combination of them, and overlapping results recorded at different sample thicknesses lead to a good approximation of the optical absorption spectrum (Figure 7).

This method could be applied as follows. First, we record the optical absorption spectrum in the wavelength region where it can easily be obtained; we record the photocurrent spectra for different sample thicknesses and for the entire wavelength range that is of interest; we fit the model on the experimental data to obtain the parameters, including  $\gamma$ , for the range where both types of spectra are available. Second, profiting from the photocurrent spectra and the model, we extrapolate the optical absorption spectrum in the wavelength range where photocurrent spectra are available, but the absorption spectrum could not be obtained by direct measurements.<sup>38</sup>

Note that the procedure can be implemented for more general integrands, and a similar method can be worked out for “parallel” arrangements as well. However, without a microscopic model these cannot account for physical processes that influence the sample absorption and are restricted to a wavelength range that is fully outside of the one covered by the recorded absorption spectrum.

**Microscopic Reaction–Diffusion Model.** The appearance of the photocurrent (photoconductivity) peak in a “perpendicular” arrangement can be explained by a microscopic model based on a reaction–diffusion system. Our model can be considered a variant of the analysis presented in ref 1 and describes the spatiotemporal evolution of the density of charge carrier pairs (electrons and holes),  $n$ , for monochromatic illumination with a certain wavelength.

We assume that the generation of charge carrier pairs in a volume element equals the product of absorbance and that of the photons reaching that site. For recombination, two possibilities are considered. The first one is given by a linear decay term. Note that decay governed by a higher power did not significantly alter the results. The second possibility is represented by a “drain” at a certain spatial location where the density of charge carrier pairs is set to be permanently zero. A diffusion term is also included, and zero-flux boundary conditions are applied. Therefore, the equations implementing the model read

$$A = \frac{0.1}{1 + \exp(0.1(\lambda - 770))}$$

$$\frac{dn(z, t)}{dt} = D \frac{\partial^2 n(z, t)}{\partial z^2} + P(z)A - \tau^{-1} n(z, t)$$

$$n(z_i) \equiv 0$$

$$j_n|_0 = j_n|_{z_{\max}} = 0$$

where  $n$  represents the density of charge carrier pairs,  $A$  the wavelength-dependent absorption,  $z$ , the recombination sites,  $j_n$  the current of the charge carrier pairs,  $P(z)$  the density of photons at depth  $z$ ,  $Z$  the sample thickness,  $D$  the effective diffusion of the charge carriers, and  $\tau$  the linear recombination rate. The discretized form of the model, as well as its computational implementation, is presented in the Supporting Information.

Numerical simulations of the microscopic model showed that for a given optical absorption spectrum the characteristics of the photocurrent peak are correlated with the sample thickness  $Z$  and the location of the recombination sites in the sample. Recombinations at the illuminated surface or close to this surface favor the increase, while recombinations farther from this surface suppress the photocurrent peak. Results of numeric simulations showing this effect are presented in Figures 8 and 9.

In the phenomenological model, the peak characteristics are influenced by the sample thickness and the parameter  $\gamma$ . This parameter is related to the distribution of the recombination sites. Even though presently we cannot quantify their relationship, interpretation of the results is obvious: If the recombination sites are placed close to the illuminated surface, where the low-wavelength light is not yet absorbed, they will significantly reduce the ability of this wavelength range to contribute to the sample conductance. In other words, they will “push down” the photocurrent spectrum in the range of the wavelengths above the band gap, emphasizing the photocurrent peak.

If the recombination sites are farther from the illuminated surface, where photons with energies slightly lower than the band gap are still able to penetrate, a near-band-gap region of the photocurrent spectrum will be suppressed (Supporting Figure S11).

Recombination sites very far from the illuminated surface, where only those photons penetrate that cannot create electrons and holes, will only slightly affect the photocurrent (photoconductivity) spectrum. In short, the microscopic explanation for the rise of the photoconductivity peak is the uneven distribution of the recombination sites across the depth of the sample; this alters the interplay between the penetration depth of the light with a certain wavelength and its ability to raise the concentration of charge carriers at a given depth. These findings enable the development of wavelength-tuned optoelectronic devices.<sup>15</sup>

## CONCLUSION

Photocurrent (photoconductivity) spectroscopy on halide perovskites has up to this time been performed only on thin layers. However, investigation of thick samples could be of special interest as well. In this paper we report the presence of a photocurrent peak in the band-gap region and model it with novel versions of the DeVore framework, emphasizing two specific experimental arrangements, namely, when the incident light beam is either parallel or perpendicular to the applied electric field.

This type of spectroscopy on thick semiconductor samples could offer a further method to determine a series of electronic properties of the investigated sample.<sup>39–41</sup> We also outline a method to obtain absorption spectra from photocurrent spectra in the sub-band-gap region. Furthermore, we provide a reaction–diffusion model on optoelectronic and recombination processes, which renders the near-band-gap photocurrent peak. We propose a cheap and simple sensor to determine the

Simulated charge carrier pair concentration ( $n$ ) units

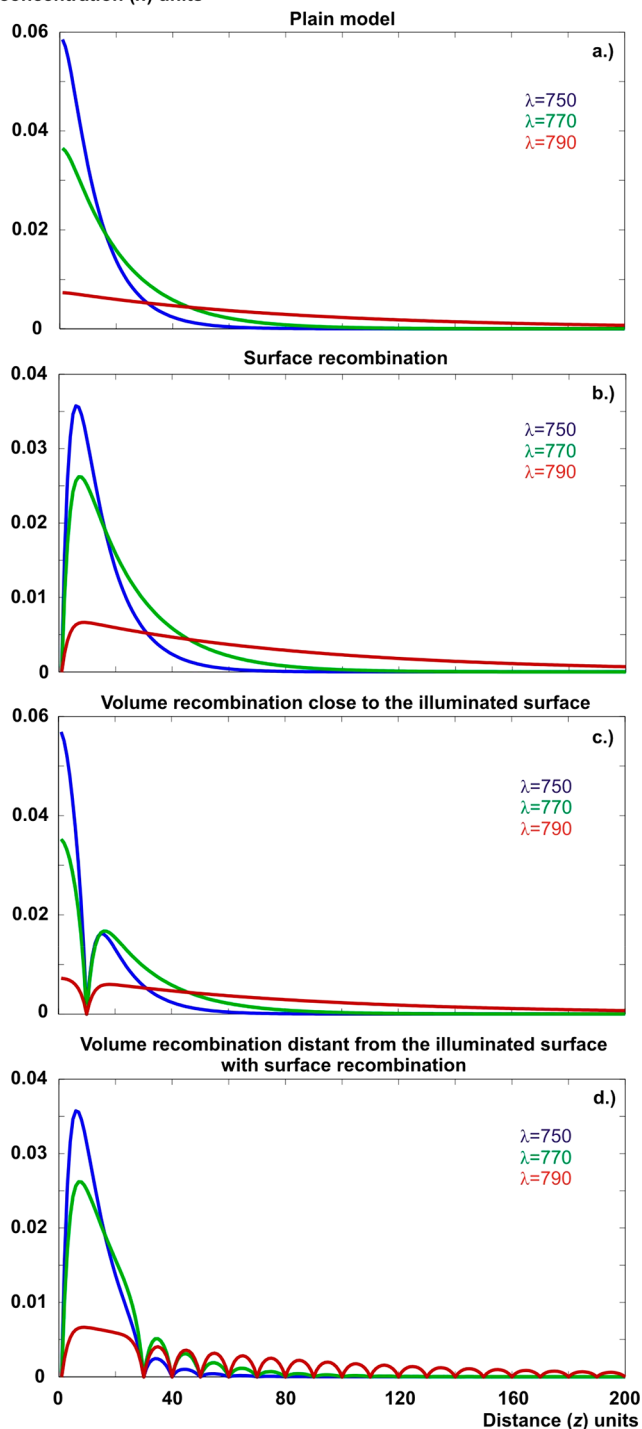


**Figure 9.** Simulated density of charge carrier pairs (electrons and holes),  $n$ , resulting from the reaction–diffusion model. The light penetrates in the sample from left, where  $z = 0$ . Blue, green, and red curves represent simulations with  $\lambda = 750$ ,  $\lambda = 770$ , and  $\lambda = 790$  wavelength units. Note the recombination sites where  $n = 0$ . Parameters are the same as for Figure 8.

direction of incidence of an electromagnetic radiation. Synthesis of MAPbI<sub>3</sub> was carried out by an efficient and simple protocol.

## ■ ASSOCIATED CONTENT

### Supporting Information

The Supporting Information is available free of charge on the ACS Publications website at DOI: 10.1021/acsp Photonics.7b00270.

Figures S1–S10, details of the experimental methods, and the core of the relevant Matlab software (PDF)

## ■ AUTHOR INFORMATION

### Corresponding Author

\*E-mail: hantz@general.elte.hu.

### ORCID

Péter Hantz: 0000-0001-5974-3755

### Notes

The authors declare no competing financial interest.

## ■ ACKNOWLEDGMENTS

We are grateful for Gy. Lakos, A. Sienkiewicz, B. Niesen, and Z. Rácz for the fruitful conversations on the model, D. Sebők for providing equipment, T. Hurtony for taking SEM images, and A. Szegedi for conducting XRD measurements. Valuable help of L. Forró, Y. Bellouard, Cs. András, G. Pintz, N. Lazányi, R. Gaal, P. Matus, M. Kollár, L. Ciric, A. Miseta, T. and Z. Bárkányi, A. Hantz, Y. Tian, K. Hegedüs, S. Bächtold, J. Spring, S. Habermacher, and Sz. Horvát is also acknowledged. The present scientific contribution is dedicated to the 650th anniversary of the foundation of the University of Pécs, Hungary.

## ■ REFERENCES

- (1) DeVore, H. B. Spectral Distribution of Photoconductivity. *Phys. Rev.* **1956**, *102*, 86–91.
- (2) Bouchenaki, C.; Ullrich, B.; Zielinger, J. P.; Nguyen Cong, H.; Chartier, P. Preparation, characterization, and bistable photoconduction of thin CdS layers. *J. Opt. Soc. Am. B* **1991**, *8*, 691–700.
- (3) Ullrich, B.; Xi, H. Photocurrent theory based on coordinate dependent lifetime. *Opt. Lett.* **2010**, *35*, 3910–3912.
- (4) Koch, S. W.; Kira, M.; Khitrova, G.; Gibbs, H. M. Semiconductor excitons in a new light. *Nat. Mater.* **2006**, *5*, 524–531.
- (5) Comin, R.; Walters, G.; Thibau, E.; Voznyy, O.; Lu, Z.-H.; Sargent, E. H. Structural, optical, and electronic studies of wide-bandgap lead halide perovskites. *J. Mater. Chem. C* **2015**, *3*, 8839–8843.
- (6) Saba, M.; Cadelano, M.; Marongiu, D.; Chen, F.; Sarritzu, V.; Sestu, N.; Figus, C.; Aresti, M.; Piras, R.; Lehmann, A. G.; Cannas, C.; Musinu, A.; Quochi, F.; Mura, A.; Bongiovanni, G. Correlated electron–hole plasma in organometal perovskites. *Nat. Commun.* **2014**, *5*, 5049.
- (7) Cadelano, M.; Saba, M.; Sestu, N.; Sarritzu, V.; Marongiu, D.; Chen, F.; Piras, R.; Quochi, F.; Mura, A.; Bongiovanni, G. *Photoexcitations and Emission Processes in: Organometal Trihalide Perovskites, Perovskite Materials—Synthesis, Characterisation, Properties, and Applications*, Likun, P., Ed.; 2016; InTech, DOI: 10.5772/61282.
- (8) Park, N.-G.; Grätzel, M.; Miyasaka, T. *Organic-Inorganic Halide Perovskite Photovoltaics, from Fundamentals to Device Architectures*; Springer, 2016.
- (9) Gao, P.; Grätzel, M.; Nazeeruddin, M. Organohalide lead perovskites for photovoltaic applications. *Energy Environ. Sci.* **2014**, *7*, 2448–2463.
- (10) Stranks, S. D.; Snaith, H. Metal-halide perovskites for photovoltaic and light-emitting devices. *Nat. Nanotechnol.* **2015**, *10*, 391–402.
- (11) Werner, J.; Weng, C.-H.; Walter, A.; Fesquet, L.; Seif, J. P.; De Wolf, S.; Niesen, B.; Ballif, C. Efficient Monolithic Perovskite/Silicon

Tandem Solar Cell with Cell Area > 1 cm<sup>2</sup>. *J. Phys. Chem. Lett.* **2016**, *7*, 161–166.

(12) Dang, Y.; Ju, D.; Wang, L.; Tao, X. Recent progress in the synthesis of hybrid halide perovskite single crystals. *CrystEngComm* **2016**, *18*, 4476–4484.

(13) Horváth, E.; Spina, M.; Szekrényes, Zs.; Kamarás, K.; Gaal, R.; Gachet, D.; Forró, L. Nanowires of Methylammonium Lead Iodide (CH<sub>3</sub>NH<sub>3</sub>PbI<sub>3</sub>) Prepared by Low Temperature Solution-Mediated Crystallization. *Nano Lett.* **2014**, *14*, 6761–6766.

(14) Sharenko, A.; Toney, M. F. Relationship between Lead Halide Perovskite Thin-Film Fabrication, Morphology, and Performance in Solar Cells. *J. Am. Chem. Soc.* **2015**, *138*, 463–470.

(15) Fang, Y.; Dong, Q.; Shao, Y.; Yuan, Y.; Huang, J. Highly narrowband perovskite single-crystal photodetectors enabled by surface-charge recombination. *Nat. Photonics* **2015**, *9*, 679.

(16) Eperon, G. E.; Stranks, S. D.; Menelaou, C.; Johnston, M. B.; Herz, L. M.; Snaith, H. Formamidinium lead trihalide: a broadly tunable perovskite for efficient planar heterojunction solar cells. *Energy Environ. Sci.* **2014**, *7*, 982–988.

(17) Park, B.; Philippe, B.; Jain, S. M.; Zhang, X.; Edvinsson, T.; Rensmo, H.; Zietza, B.; Boschloo, G. Chemical engineering of methylammonium lead iodide/bromide perovskites: tuning of optoelectronic properties and photovoltaic performance. *J. Mater. Chem. A* **2015**, *3*, 21760–21771.

(18) De Wolf, S.; Holovsky, J.; Moon, S. J.; Löper, P.; Niesen, B.; Ledinsky, M.; Haug, F.-J.; Yum, J.-H.; Ballif, C. Organometallic Halide Perovskites: Sharp Optical Absorption Edge and Its Relation to Photovoltaic Performance. *J. Phys. Chem. Lett.* **2015**, *5*, 1035–1039.

(19) Tian, Y.; Scheblykin, I. G. Artifacts in Absorption Measurements of Organometal Halide Perovskite Materials: What Are the Real Spectra? *J. Phys. Chem. Lett.* **2015**, *6*, 3466–3470.

(20) Ikuno, T.; Hasegawa, M. Wavelength-dependent switching of photocurrent polarity in a semiconductor film with bifacial band bendings. *Appl. Phys. Express* **2016**, *9*, 062201.

(21) Ball, D. J. *The Basics of Spectroscopy*; SPIE Press, 2001.

(22) Studenyak, I.; Kranjčec, M.; Kurik, M. Urbach Rule in Solid State Physics. *Int. J. Opt. Appl.* **2014**, *4*, 76–83.

(23) De Laurentis, M.; Irace, A. Optical Measurement Techniques of Recombination Lifetime Based on the Free Carriers Absorption Effect. *J. Solid State Phys.* **2014**, *2014*, 291469.

(24) Turkulets, Y.; Bick, T.; Shalish, I. Double surface effect causes a peak in band-edge photocurrent spectra: a quantitative model. *J. Phys. D: Appl. Phys.* **2016**, *49*, 365104.

(25) Hantz, P.; Plesz, B.; Sipos, Á.; Jalsovszky, I. Method for determining incidence direction of an electromagnetic beam, Priority 27 February 2017. Hungarian Patent Application, Provis. No. P1700328, July 2017.

(26) Molnar, A.; Wang, A.; Gill, P. Light field image sensor, method and applications. U.S. Patent Application 20150125943, 2015.

(27) Yamada, M.; Maeda, Y.; Nakamura, M.; Terada, T.; Shirai, M. Photosensor for detecting the position of incident light in two dimensions using a pair of film resistors and a photoconductive element sandwiched between. U.S. Patent 5517017, 1996.

(28) Levinton, D. B. Apparatus and method for a light direction sensor. U.S. Patent 7924415, 2011.

(29) Varghese, V.; Chen, S. Incident light angle detection technique using polarization pixels. *IEEE SENSORS 2014 Proceedings, Valencia*, **2014**; pp 2167–2170.10.1109/ICSENS.2014.6985468.

(30) Wang, H.; Luo, T.; Song, H.; Christen, J. B. On-chip sensor for light direction detection. *Opt. Lett.* **2013**, *38*, 4554–4557.

(31) Hegyi, D. System for determining the direction of incident optical radiation. U.S. Patent 5264691, 1993.

(32) Náfárdi, B.; Náfárdi, G.; Forró, L.; Horváth, E. Methylammonium Lead Iodide for Efficient X-ray Energy Conversion. *J. Phys. Chem. C* **2015**, *119*, 25204–25208.

(33) Wei, H.; Fang, Y.; Mulligan, P.; Chuirazzi, W.; Fang, H.-H.; Wang, C.; Ecker, B. R.; Gao, Y.; Loi, M. A.; Cao, L.; Huang, J. Sensitive X-ray detectors made of methylammonium lead tribromide perovskite single crystals. *Nat. Photonics* **2016**, *10*, 333–339.

(34) Schemm, N.; Balkır, S.; Hoffman, M. W.; Bauer, M. A. Directional Gamma Ray Detector Using a Single Chip Computational Sensor, **2011**, *IEEE Sensors*.176010.1109/ICSENS.2011.6127024

(35) Yakunin, S.; Dirin, D.; Shynarenko, Y.; Morad, V.; Cherniukh, I.; Nazarenko, O.; Kreil, D.; Nauser, T.; Kovalenko, M. V. Detection of gamma photons using solution-grown single crystals of hybrid lead halide perovskites. *Nat. Photonics* **2016**, *10*, 585–590.

(36) Becker, E. M.; Farsoni, A. T. A multi-panel direction-sensitive gamma-ray detector for low-altitude radiological searches, Nuclear Instruments and Methods in Physics Research Section A. *Nucl. Instrum. Methods Phys. Res., Sect. A* **2016**, *836*, 13–21.

(37) Holovsky, J. Fourier Transform Photocurrent Spectroscopy on Non-Crystalline Semiconductors. In *Fourier Transforms - New Analytical Approaches and FTIR Strategies*, [www.intechopen.com/books/fourier-transforms-new-analytical-approaches-and-ftir-strategies](http://www.intechopen.com/books/fourier-transforms-new-analytical-approaches-and-ftir-strategies) (accessed Dec 1, 2017).

(38) Hantz, P.; Plesz, B.; Sipos, Á.; Jalsovszky, I. Method for approximate determination of optical absorption spectra from photocurrent spectra. Hungarian Patent Application, Provis. No. P1700327, July 2017.

(39) Franc, J.; Hildek, P.; Belas, E.; Linhardt, V.; Popisil, S.; Grill, R. Photoconductivity spectroscopy of deep levels in CdTe. *IEEE Trans. Nucl. Sci.* **2005**, *52*, 1956–1960.

(40) Klots, A. R.; Newaz, A. K. M.; Wang, B.; Prasai, D.; Krzyzanowska, H.; Lin, J.; Caudel, D.; Ghimire, N. J.; Yan, J.; Ivanov, B. L.; Velizhanin, K. A.; Burger, A.; Mandrus, D. G.; Tolks, N. H.; Pantelides, S. T.; Bolotin, K. I. Probing excitonic states in suspended two-dimensional semiconductors by photocurrent spectroscopy. *Sci. Rep.* **2015**, *4*, 6608.

(41) Amirtharaj, P. M.; Seiler, D. Optical properties of semiconductors. In *Handbook of Optics*; McGraw-Hill: New York, 2009; Chapter 36.